Ultrafast Harmonic Coherent Compound (UHCC) imaging for high frame rate echocardiography and Shear Wave Elastography

Mafalda Correia[1], **Jean Provost**[1], **Simon Chatelin**[1], **Olivier Villemain**[1], **Mickael Tanter**[1], and **Mathieu Pernot**[1]

[1]Institut Langevin, ESPCI ParisTech, CNRS UMR 7587, INSERM U979, Paris, France, Université Paris Diderot-Paris7, Paris, France

Abstract

Transthoracic shear wave elastography of the myocardium remains very challenging due to the poor quality of transthoracic ultrafast imaging and the presence of clutter noise, jitter, phase aberration, and ultrasound reverberation. Several approaches, such as, e.g., diverging-wave coherent compounding or focused harmonic imaging have been proposed to improve the imaging quality. In this study, we introduce ultrafast harmonic coherent compounding (UHCC), in which pulse-inverted diverging-waves are emitted and coherently compounded, and show that such an approach can be used to enhance both Shear Wave Elastography (SWE) and high frame rate B-mode Imaging. UHCC SWE was first tested in phantoms containing an aberrating layer and was compared against pulse-inversion harmonic imaging and against ultrafast coherent compounding (UCC) imaging at the fundamental frequency. In-vivo feasibility of the technique was then evaluated in six healthy volunteers by measuring myocardial stiffness during diastole in transthoracic imaging.

We also demonstrated that improvements in imaging quality could be achieved using UHCC B-mode imaging in healthy volunteers. The quality of transthoracic images of the heart was found to be improved with the number of pulse-inverted diverging waves with reduction of the imaging mean clutter level up to 13.8-dB when compared against UCC at the fundamental frequency. These results demonstrated that UHCC B-mode imaging is promising for imaging deep tissues exposed to aberration sources with a high frame-rate.

Introduction

Myocardial stiffness evaluation could help to assess and diagnose several pathologies associated with elasticity changes, such as ischemia, cardiomyopathies and heart failure. However, as of today, myocardial stiffness cannot be measured non-invasively in clinical practice. In the past decades, ultrasound [1]–[7] and magnetic resonance [8]–[10] elastography imaging techniques have been proposed and developed to evaluate tissue stiffness properties. Techniques are typically based on the mapping of the propagation of mechanical waves in tissue; more specifically, low-frequency shear waves are induced and tracked in order to estimate their propagation speed (which typically lies between 1 and 10 m/s). Specifically, ultrasound shear-wave elastography (SWE) consists in 1) generating a push using acoustic radiation force, 2) image the resulting shear-wave propagation and 3)

map the local velocity of the shear wave, which can be used to determine the local stiffness of tissues using rheological models of varying complexities.

Recent advances in the elastography techniques have allowed for stiffness measurements in deep organs, such as the heart, [11]–[16]. Indeed, several in-vivo shear wave elastography studies have shown in open chest animals that local stiffness measurements, during one cardiac cycle, are feasible and clinically relevant [17]–[19]. A high imaging frame rate is required, i.e., typically above 1000 frames/s, in order to track shear waves induced in the human heart. Different approaches were proposed to achieve such frame rates, such as, ECG-gated [20], [21], and ultrafast imaging with unfocused transmit waves [22]–[26]. However, transthoracic shear wave Imaging remains challenging in-vivo for multiple reasons. First, the presence of clutter noise, jitter, phase aberrations, and ultrasound reverberation reduce the imaging quality due to distortion of the transmitted pulses. Second, ultrasound attenuation reduces the signal-to-noise ratio of the tissue velocities used to track the shear wave. Recent studies have shown, independently, that harmonic imaging [27] and coherent compounding [28] could palliate these two issues.

Harmonic imaging uses the non-linear propagation of ultrasound wave to improve image quality [29]. Indeed, many factors, such as, e.g., the presence of fat, skin layer thickness, and hydration level result in the progressive distortion of ultrasound waves as they propagate into the tissue. This distortion leads to imaging artifacts, such as, e.g., clutter noise, jitter, phase aberration, and ultrasound reverberation. Harmonic imaging provided a reduction of these artifacts by using a lower frequency in transmit but without compromising on contrast and resolution [30]. The non-linear propagation of ultrasound waves, in biological tissues, generates harmonic frequencies that are multiple integers of the fundamental transmitted-wave frequency. To perform harmonic imaging, one must isolate the higher harmonic signals contained in the backscattered ultrasound echoes, and different methods typically based on filtering and pulse-inversion have been proposed to do so [30]. Indeed, a band-pass filter [31] can be directly applied onto the baseband signals to isolate the 2nd harmonic content. In Pulse-Inversion (PI) techniques [32], two identical pulses of opposite polarity are sequentially transmitted. Their respective received signals are then summed, which results in the cancellation of linear and odd harmonic components and in the doubling of the even harmonic components. The PI method is often preferred as it has the advantage of cancelling harmonic content generated by the electronics. However, since two pulses are summed to form a single image, PI divides the imaging frame rate by two.

While harmonic imaging techniques have been used extensively for B-mode and contrast imaging, their application to SWE is relatively recent. Song *et al.* [27] proposed a pulse-inversion harmonic sequence with unfocused emissions for SWE, using a phased-array transducer to improve transthoracic cardiac shear wave measurements. Also, Doherty *et al.* [33] proposed a fully-sampled sliding-window pulse-inversion harmonic technique, that decreases jitter and does not divide by half the imaging frame-rate, to arterial Acoustic Radiation Force Impulse Imaging improvement. Both works showed an improvement of the tissue velocity estimation, indicating that harmonic imaging for cardiac transthoracic applications can contribute to improve shear wave tracking and, as a consequence, myocardial stiffness measurements.

Approaches based on the coherent compounding of successive backscattered echoes, such as, e.g., as synthetic aperture imaging [34] and plane-wave coherent compounding [35], have been proposed to improve image quality and motion estimation. For instance, in plane-wave coherent compounding, the backscattered echoes from successive tilted plane waves transmitted at high frame rate are coherently compounded to restore a synthetic focus in transmit. Recently, this principle was extended to diverging-waves [28] in order to achieve larger fields-of-view using ultrafast ultrasound imaging in cardiac applications. This approach is similar to synthetic aperture imaging when a small number of virtual sources positioned behind the probe are used [36].

Based on our previous work [28], we propose to combine the coherent compounding approach with harmonic imaging, using a sliding-window pulse-inversion approach, with the objective of improving transthoracic ultrafast imaging of the heart. In this study, we demonstrate that by combining the two techniques, larger signal-to-noise ratio and reduced clutter and aberration noise can be obtained.

Specifically, we propose two implementations of Ultrafast Harmonic Coherent Compound (UHCC) Imaging: one for Cardiac SWE, and another for high frame-rate B-mode imaging. UHCC SWE was designed for enhanced shear wave propagation tracking and thus is performed at very high frame-rate. We showed herein that UHCC SWE improves the signal-to-noise ratio of shear wave velocity mapping, when compared against ultrafast coherent compound (UCC) imaging at fundamental frequency [28] and sliding-window pulse-inversion harmonic (UH) Imaging [33] in a pork-belly-gelatin-agar phantom. The in vivo feasibility of UHCC SWEI was evaluated on the heart, by measuring the diastolic myocardial stiffness transthoracically of six healthy volunteers. UHCC B-mode Imaging was designed to improve imaging quality at large field-of-view and high frame-rate, and evaluated in-vivo in healthy volunteers. We showed that UHCC B-mode Imaging is more efficient for clutter noise reduction than UCC B-mode imaging at the fundamental frequency.

Materials and Methods

An Aixplorer system (Supersonic Imagine, Aix-en-Provence, France) and a 2.75-MHz linear phased-array transducer (Vermon S.A., Tours, France, 96 elements, 0.2-mm pitch) were used for B-mode and SWE acquisitions. Two sequences based on ultrafast imaging [28] were designed: a first sequence dedicated to shear wave elastography imaging, and a second to perform B-mode imaging. The two sequences were built with similar transmit patterns and were adapted according to the constraints of each imaging mode.

1   Imaging Sequences

The imaging sequences developed herein are based on the emission of diverging waves. Diverging waves are defined by a virtual source located behind the probe and are associated with an emission subaperture. These diverging waves emanating from different virtual sources can then be coherently summed, and image quality can be improved (see Papadacci et al. [28] for details).

For each imaging mode, a different diverging-waves transmission sequence was designed. SWE requires a high frame rate for the tracking of the propagation of shear waves. Hence, a small number of virtual sources were used in SWE sequences. To increase the relatively limited signal-to-noise ratio associated with a small number of virtual sources, the virtual sources can be positioned farther behind the probe to increase the radius of the diverging wave, which allows for a larger number of elements contributing to the emission and limits the geometrical attenuation. The trade-off, however, is a reduced field-of-view. In the case of B-mode imaging, a large number of virtual sources positioned near the probe were used in order to achieve a large field-of-view and high contrast imaging, at the cost of a reduced frame rate.

To perform harmonic imaging, the emission associated with each virtual source was performed twice, with opposite polarities.

a)   UHCC SWE Imaging—A shear wave was generated using a push beam with a 2.75-MHz central frequency with full aperture, i.e., using all of the 96 elements of the probe. Immediately after generating the shear wave, the UHCC imaging sequence was launched. In this sequence, N virtual sources were used with a full aperture, i.e., with all 96 elements). The set of N diverging waves was transmitted (center frequency = 1.9-MHz, pulse duration = 2 cycles) by organizing the virtual sources (indicated by i = 1,…, N in figure 1) in a virtual array with a pitch equal to 96/N elements (see figure 1), and at a 30-mm distance behind the probe. For each virtual source, diverging waves of opposite polarity were emitted sequentially and the backscattered RF signals associated with both polarities were recorded and summed using a sliding window [33]. Finally, by coherently recombining each harmonic data set associated with different virtual sources, compounded harmonic images were produced with a frame rate equal to the pulse repetition frequency. From these images, 2-D axial tissue displacements maps were obtained using a table-sum 1-D RF cross-correlation with cosine interpolation applied onto RF data [37], [38]. After compounding of the images associated with each virtual source, the resulting frame rate was therefore given by

$$FR = \frac{PRF}{N},$$

where *PRF* is the pulse repetition frequency and *N* is the number of coherently compounded diverging waves. The frame rate achieved was therefore equal to the one in the UCC imaging sequence [28].

The time sequence of an UHCC SWE acquisition is summarized in figure 1, in which an example using three diverging waves is provided. In this study, the UHCC was compared against other previously published techniques, which correspond to UHCC without the use of either pulse inversion (UCC) or coherent compounding (UH), respectively.

b)   UHCC B-mode imaging—For B-mode imaging, a set of *N* diverging-waves was transmitted (center frequency = 1.9-MHz, pulse duration = 2 cycles) using a 21-element subapertures. The virtual sources were arranged in a virtual 1-D array by positioning each virtual source (*i = 1,…,N*) at the center of a (96/*21*)-element subaperture (figure 2), i.e. 4.2-

mm distance space, and at a 3-mm distance behind the ultrasound probe. For each virtual source, diverging waves of opposite polarity were emitted sequentially and backscattered RF signals from each polarity were received and summed. Unlike Ultrafast Harmonic Coherent Compound SWE sequence no sliding-window sum was applied. By coherently recombining each *N*-harmonic data set, compounded images were produced. The resulting frame rate *FR* is given by

$$FR = \frac{PRF}{2 \times N}$$

where *PRF* is the pulse repetition frequency and *N* is the number of coherently compounded diverging waves. The B-mode Ultrafast Harmonic Coherent Compound Imaging sequence is summarized in figure 2, using a 3 diverging-waves example.

2   In-vitro Experimental setup

Pork-belly/Gelatin-Agar phantom Fundamental and Harmonic coherently compounded diverging-waves SWE studies—Experiments to quantify the image quality of UHCC SWE were performed in a pork-belly-gelatin-agar phantom (7% gelatin, 2% Agar and 1% propanol), with two different experimental apparatus.

In the first experimental apparatus, an absorber made of polyurethane (NPL, UK) was covered with a gelatin-agar layer to create a gelatin-agar phantom (figure 3-A) that mimics an ideal homogeneous soft tissue.

In the second one, a fresh piece of pork-belly skin with fat was positioned above the gelatin-agar (figure 3-B). The pork-belly skin layer allowed us to generate ultrasound aberrations similar to the ones caused in-vivo.

In both experimental apparatus, the probe was positioned on top of the phantoms immersed in a layer of water, to guarantee good acoustic coupling.

In all the in vitro experiments, a shear wave was generated using a 300-us-long, 2.75-MHz push-beam focused at 65 mm below the center of the transducer. Six different sequences to track the shear wave during 7 ms were compared in the two phantom configurations. Specifically, three different sequences with *N* = 1, 2 and 3 coherently compounded diverging waves were designed, with and without pulse-inversion, i.e. UHCC and UCC sequences. The imaging depth was fixed to 90 mm and the *PRF* to 5924 Hz. For the fundamental sequences (i.e., without pulse-inversion), a 2.75-MHz center frequency was used. In the case of harmonic sequences, a 1.9-MHz center frequency was used in transmit and a 3.8-MHz frequency was used in receive. Each sequence was repeated 5 times. Additionally, prior to the shear wave imaging sequence, a UHCC B-mode image was obtained using 10 coherently compounded diverging waves.

3   In-vivo human heart experimental setup

The in vivo feasibility was assessed by performing transthoracic human heart SWE and B-mode imaging in six healthy volunteers. All volunteers signed an informed consent and the

research study was performed within the clinical investigation protoc0ol n° 2015-A00187-42 approved by the CPP (Comité de Protection des Personnes), Ile de France VI, France. The acoustic output of the sequences used in-vivo was measured using a calibrated interferometer in water. The ultrasonic sequences complied with the Food and Drug Administration (FDA) requirements (510k Track 3, FDA) regarding the mechanical Index (MI) and the spatial-peak time average (I_{SPTA}) with the derating factor of 0.3 dB cm^{-1}MHz^{-1}. In the SWE imaging sequence, the $MI_{0.3}$ was limited by the pressure at the focus of the push beam and it was set to 1.8. The $I_{SPTA0.3}$ was 154 mW/cm2, assuming a repetition time of 1 second. For the unfocused transmits, the $MI_{0.3}$ and $I_{SPTA0.3}$ were 0.6 and 0.54 mW/cm2, respectively assuming a repetition time of 1 second. For both imaging acquisitions, $MI_{0.3}$ and $I_{SPTA0.3}$ values were inferior to $MI_{0.3}$ = 1.90 and $I_{SPTA0.3}$ = 720 mW/cm^2, limits imposed by the FDA. The temperature at the probe surface was also measured and remained stable for the transmission of one SWEI (20-ms duration) and B-mode imaging (15-ms duration) sequences repeated every second. The increased temperature was inferior to temperature uncertainty of the measurement system (±0.1 °C) during the sequences tests.

The experiments were conducted and performed by a trained cardiologist. A parasternal short-axis view was used for all the acquisitions. The time between each acquisition was 1 minute. Repeatability was assessed in one volunteer by performing 5 successive acquisitions separated by one minute.

a) Transthoracic UHCC SWE study—A push-beam of 2.75-MHz central frequency and 300 μs duration was induced in the center of the anteroseptal myocardial wall of the left ventricle. The focal depth was adjusted for each patient between 45 and 75 mm in order to position the focal zone at the midwall location of the anteroseptal wall. The UHCC SWE sequences were set to one, two and three diverging-waves transmission with a PRF of 6849 Hz. They were synchronized with the ECG signal in order to generate and detect shear wave motion at end-diastole.

A prior to the UHCC SWE acquisition, a UHCC B-mode imaging was also obtained with the following parameters: 15 diverging waves, at a 120-mm depth, and a frame-rate equal to 153 frames/s (PRF = 4608 Hz).

b) UHCC and UCC B-mode Imaging – diverging-waves coherently compounded number evaluation—To evaluate the imaging quality in terms of SNR and contrast, experiments were performed using a UHCC B-mode imaging sequence and compared against the performances of UCC. For both sequences, i.e. UHCC and UCC, the transmission was performed using one to 40 coherently compounded diverging waves, at a 100-mm depth and with a PRF equal to 5319 Hz. The imaging frame-rate varied between 5319 and 133 frames/s for the UCC sequence. For the same number of coherently compounded diverging waves, the frame-rate was divided by half for UHCC.

4 Post-processing analysis

Beamforming of radio-frequency (RF) signals was performed using a conventional delay-and-sum algorithm implemented on the GPU.

a)   Shear Wave Propagation Tracking and speed estimation—Tissue axial velocity images were obtained using 1-D cross-correlation of successive frames with cosine interpolation applied on the beamformed RF signals [37], [38]. A 1.5-mm kernel size with a 97.5-% overlap was used for all sequences. Tissue velocity images were then scan-converted. Spatiotemporal tissue velocity data was then computed and shear wave speeds in the –x and +x directions were assessed using a linear least-squares estimation on temporal 1-D cross-correlation with different lateral spatial lags (lags range: 1 to 10 pixels) [39].

For the in-vitro experiments, the shear wave speed was estimated using the spatiotemporal tissue velocity data that were averaged within depths of 3-mm around the push location.

In these experiments, the signal-to-noise ratio (SNR) was evaluated quantitatively around the push region for UCC and UHCC SWE studies. SNR maps were calculated, as follows:

$$SNR_{dB} = 10 log_{10} \frac{\sum_{t=0}^{T} S(x,z,t)^2}{\sigma_{xz}^2},$$

where S the tissue velocity image, σ_{xz} is the tissue velocity standard deviation in absence of shear wave propagation, and T the acquisition time. The averaged SNR values were evaluated within a region-of-interest around the push location. The percentage of area within these regions-of-interest with a SNR above a threshold of 25 dB was quantified. This threshold was determined by Deffieux et al. [40] as an acceptable SNR for the reconstruction of shear velocity maps with a standard-deviation of 10%.

For the in-vivo acquisitions, the average myocardial wall motion was subtracted before the tissue velocity images scan conversion, since the natural myocardial wall has a low frequency content [41], [42] and acts as a noise source in the detection of the shear wave propagation. Also, the anteroseptal wall was segmented to using a B-mode image reference acquired.

Then, the shear wave speed in the –x and +x directions was estimated, through spatiotemporal tissue velocity data that were averaged within depths of 3-mm around the push location in the anteroseptal wall. Shear wave speeds were assessed and the adjusted coefficient of determination $\left(\overline{R}^2 \right)$ of the least-squares fit results was calculated. The adjusted coefficient of determination was used as an exclusion criteria for the shear wave speed estimation. Values with an adjusted coefficient of larger than 80% of the shear wave speed estimation were excluded and no shear wave propagation was considered in those cases.

b)   UHCC and UCC B-mode Imaging—The B-mode image quality was assessed on the final images, i.e., after beamforming, coherent summation, scan conversion and log-compression, with a 60-dB dynamic range. Then, in order to evaluate imaging quality in function of the number of diverging-waves emitted, a mean clutter level analysis in regions-of-interest were performed, for both UHCC and UCC sequences. These regions-of-interest $(5 \times 6 \text{ mm}^2)$ were chosen and positioned arbitrarily in the anterior and posterior wall, and in the left ventricle cavity at approximately the same depth to evaluate the contrast of the

image. For each region-of-interest, the absolute intensity values of ultrasound images was averaged over the region of interest. Finally, the mean clutter level for UHCC and UCC was determined by the ratio of the average intensity in the cardiac cavity and in the tissue.

Results

1   In-vitro acquisitions

a)   Gelatin-Agar/ Pork-belly-gelatin-agar phantoms Fundamental and Harmonic coherent compound diverging-waves SWE studies—Figure 4 presents the results acquired for the gelatin-agar phantom. Acquisitions provided an image quality that was sufficiently high for the estimation of the shear wave speed, regardless of the number of compounded diverging waves or of the use of pulse inversion.

Figure 5 shows the results obtained with this pork-belly-gelatin-agar phantom.

Shear wave propagation tracking was possible for all acquisitions. However, in this case, due to the skin and fat layer, which causes ultrasound aberrations, the UHCC sequence resulted in a qualitatively larger signal-to-noise ratio. Indeed, one can observe that the waveform is better defined with respect to the background noise and especially at larger propagation distances when using UHCC.

Figure 6, 7, and table 3 provide a systematic and quantitative analysis of this observation. The percentage of area with a SNR above a threshold of 25 dB was quantified and is showed as well in table 3.

Figure 6 shows that the SNR is relatively similar when using the UCC and UHCC sequences in the gelatin-agar phantom configuration. We also note that the SNR increases with the number of compounded diverging waves, as was demonstrated previously in another study [28].

Figure 7, on the other hand, shows that in presence of an aberrating layer such as a pork-belly layer and for a fixed number of compounded diverging waves, the SNR associated with UHCC is larger than the SNR associated the UCC sequence.

Table 3 summarizes these results using the spatial average of the SNR maps of the regions-of-interest shown in figure 6 and 7. Interestingly, in absence of an aberrating layer (i.e., when using the gelatin-agar phantom), the SNR associated with the UHCC sequence was relatively equivalent with the SNR associated with the UCC sequence, albeit by a small value (0.7 dB when using two and three coherently compounded diverging waves). Also, the area above 25-dB was almost 100% using both UHCC and UCC. In contrast, the UHCC sequence provided a consistent improvement in SNR in presence of an aberrating layer, i.e. pork-belly-gelatin-agar phantom. This improvement was larger in absolute difference of SNR when increasing the number of diverging waves, but the relative improvement was approximately constant (approx. 30.6 % SNR improvement when compared against UCC for a fixed number of compounded diverging waves). The SNR surface area percentage above 25-dB was higher for UHCC than UCC and increased consistently with 2 and 3 coherently compounded diverging waves.

2   *In-vivo* acquisitions

a)   Transthoracic UHCC SWE in the Human Heart—UHCC SWE was evaluated in-vivo at high frame rates (>1500 frames/s), using 1, 2 and 3 diverging-waves. The spatiotemporal axial tissue displacements images, averaged within 3-mm depth around the myocardial wall center are shown in figure 8 for the six volunteers.

Without coherent compounding, shear wave imaging the shear wave propagation was detected in volunteers 1 (in both directions), 2 (in both directions), and 6 (in +x direction). Using two compounded diverging waves, the shear wave propagation was detected in all volunteers in at least one direction. Using three diverging waves, shear waves were detected in all acquisitions in both directions, except in volunteer 6, where no shear wave was detected.

The shear wave speed was estimated for all the acquisitions where shear waves could be tracked in at least one direction.

After the applicability of the exclusion criteria, shear wave propagation speeds were estimated in all cases, with the exception of the volunteers 4 (in -x direction) and 6 (in –x direction). These results are shown in table 4.

Repeatability tests were performed in one volunteer. The UHCC sequence was repeated five times for 1, 2, and 3 compounded diverging waves and shear waves were tracked for both –x and +x directions. In each acquisition, spatiotemporal images were computed, averaged within a 3-mm deep region, and centered in the left-ventricle anterior-septal midwall. Arithmetic means and standard deviations are presented in table 5.

b)   Transthoracic B-mode Human Heart study—UHCC B-mode imaging was evaluated using 1 to 40 coherently compounded diverging waves transmission, and compared against UCC B-mode. Figure 9 shows the imaging quality improvement of the UCC and UHCC B-mode images with an increasing number of diverging-waves. As indicated by a previous study [43], increasing the number of compounded diverging waves resulted in improvements in terms of SNR, lateral resolution, and contrast when compared with a single diverging wave image.

The mean clutter value in the cardiac cavity (regions-of-interest represented by red boxes) was also evaluated and results are presented in figure 9.

The contrast of UHCC B-mode Imaging was consistently larger than UCC B-mode Imaging. Specifically, a clutter level decrease of 6.3-dB was found for one diverging wave and 13.8-dB for 40 diverging waves compared against UCC imaging with the same number of transmitted waves.

Discussion

This paper investigated the potential of a hybrid ultrafast imaging sequence based on the combination of pulse inversion and coherent compound imaging. Two sequences were designed and implemented in-vivo: UHCC SWE and UHCC B-mode imaging. The main

aim of this study was to assess the potential of UHCC as a means to improve shear wave tracking in transthoracic cardiac applications that suffer from different noise sources.

UHCC SWE was first evaluated in an in-vitro study. Harmonic imaging alone was shown to improve the shear wave tracking in the presence of an aberrating layer composed of porcine fat-and-skin. Combining the coherent compounding approach allowed for a larger signal-to-noise ratio. The feasibility of UHCC SWE was assessed in transthoracic imaging of the human heart. Experiments were performed in six healthy volunteers during end-diastole in the left-ventricle anteroseptal wall. The acquisitions were performed during end-diastole, i.e., when the myocardium is relatively soft and the shear wave speed is typically in the 1-2 m/s range. The reproducibility of the presented technique was assessed in one volunteer by performing 5 acquisitions. Results showed that shear wave tracking is possible by the combination of harmonic imaging and coherent compound imaging with diverging waves. Up to three diverging waves were used. Variations between +x and –x direction were also found, as expected, due to the complexity and anisotropy of myocardium tissue in the anteroseptal wall, composed of an arrangement of fibers from left and right ventricles.

In this study, compound imaging was shown to improve SWE on phantoms and was feasible in vivo on most acquisitions. However, UHCC SWE remains challenging in vivo, the signal to noise ratio was much lower than in the in vitro acquisitions and shear velocity estimation was not possible for every acquisitions. Therefore, further investigation are required to show that it can be applied in clinical practice and to determine the optimal number of diverging waves.

The maximum number of coherently compounded diverging waves is indeed limited by the shear wave speed. The trade-off between the number of coherently compounded diverging waves and the temporal sampling in SWE depends on many parameters including the tissue stiffness and the probe parameters and is complex to quantify. This study suggests that for shear wave speeds of a few meters per second, 3 pulse-inverted coherently compounded diverging waves (i.e., corresponding to 6 emissions) can be used for diastolic shear wave propagation tracking. For a PRF of 5924 frames/s, this corresponds to a frame-rate of 1916 frames/s.

In systole, the heart contracts and, as a result, the shear wave speed is comparatively higher. To estimate the systolic shear wave speed, higher frame rates are required, or, equivalently, a smaller number of coherently compounded diverging waves should be used, which, in turn, reduces the SNR. The twisting of the heart during systole could also exacerbate artifacts associated with out-of-plane motion. The in-vivo shear wave elastography studies in open chest animals [17]–[19] have shown that shear wave speed in systole is at least 3 times higher compared against the diastolic shear wave speed (shear wave speed in the 5-6 m/s range). Consequently for a PRF of 5924 frames/s, the frame-rate necessary to track shear wave speed in systole could reach 5924 frame/s, which corresponds to 1 diverging-wave transmission.

When using such a small number of emissions, it can be shown [28] that the influence of fast cardiac tissue motion degrades the coherence of the compound operation only in a limited

and for most practical aspects, negligible. However, for a larger number of compounded diverging waves a motion correction factor should be considered, as proposed previously [44].

It should also be noted that even if all the acquisitions were performed by a trained cardiologist differences between acquisitions could occurred due to patient breathing or sonographer's motion.

This study was focused on the challenging application of myocardial shear wave elastography. However, UHCC could benefit and be applied to other applications that have limited imaging quality due to attenuation and aberrations, such as in liver SWE. These sequences could also be implemented in conventional linear arrays by replacing the emission of diverging waves with plane-waves.

UHCC B-mode imaging was also implemented and evaluated in-vivo. A comparison of the technique against UCC was performed to assess differences in contrast, SNR and axial resolution.

Regarding clutter noise reduction, contrast increase, and axial resolution improvement, the combination of harmonic imaging with ultrafast coherent compound imaging allowed for a strong increase in image quality when compared against the fundamental imaging. In this method, no sliding-window was applied to privilege the pulse-inversion effect instead of imaging frame-rate, unlike in the UHCC SWE sequence. Using coherent compounding, the tradeoff between frame-rate and image quality can be adjusted at no expense in terms of field of view. B-mode images with good image quality can be obtained at a frame-rate of 270 frames/s for 10 coherently compounded diverging-waves and for 10 cm of depth. These results are promising for imaging deep tissues exposed to aberration sources in cardiac applications but also for the imaging of the liver in patients with high body mass index.

Conclusion

In this study, we combined harmonic imaging and coherent compounding ultrafast imaging and applied it to cardiac SWE and high frame rate B-mode imaging. The sequences were implemented on an ultrasound scanner and experiments were performed with a phased-array probe. Image quality and shear wave propagation detection was evaluated by comparing the technique with the fundamental approach. Experiments performed through an aberrating layer, showed that shear wave propagation tracking was improved by both harmonic imaging and coherent compounding and even more by the combination of both techniques, with UHCC imaging. Improvements in signal-to-noise ratio were quantified and consistent in all *in-vitro* experiments. In-vivo feasibility was shown in the human heart, to measure non-invasively shear waves speeds of the left ventricle wall and to evaluate B-mode image quality improvement. This technique could be used to perform shear wave imaging and to improve B-mode imaging in the human heart.

Acknowledgements

References

1. Fatemi M, Greenleaf JF. Vibro-acoustography: an imaging modality based on ultrasound-stimulated acoustic emission. Proc Natl Acad Sci U S A. 1999 Jun; 96(12):6603–8. [PubMed: 10359758]

2. Catheline S, Thomas J, Wu F, Fink MA. Diffraction Field of a Low Frequency Vibrator in Soft Tissues Using Transient Elastography. IEEE Trans Ultrason Ferroelectr Freq Control. 1999; 46(4): 1013–1019. [PubMed: 18238506]

3. Sandrin L, Fourquet B, Hasquenoph J-M, Yon S, Fournier C, Mal F, Christidis C, Ziol M, Poulet B, Kazemi F, Beaugrand M, et al. Transient elastography: a new noninvasive method for assessment of hepatic fibrosis. Ultrasound Med Biol. 2003 Dec; 29(12):1705–1713. [PubMed: 14698338]

4. Sarvazyan AP, Rudenko OV, Swanson SD, Fowlkes JB, Emelianov SY. Shear Wave Elasticity Imaging: A new ultrasonic technology of medical diagnostic. Ultrasound Med Biol. 1998; 24(9): 1419–1435. [PubMed: 10385964]

5. Nightingale K, Soo MS, Nightingale R, Trahey G. Acoustic radiation force impulse imaging: in vivo demonstration of clinical feasibility. Ultrasound Med Biol. 2002 Feb; 28(2):227–35. [PubMed: 11937286]

6. Bercoff J, Tanter M, Fink M. Supersonic shear imaging: a new technique for soft tissue elasticity mapping. IEEE Trans Ultrason Ferroelectr Freq Control. 2004 Apr; 51(4):396–409. [PubMed: 15139541]

7. Song P, Zhao H, Manduca A, Urban MW, Greenleaf JF, Chen S. Comb-push ultrasound shear elastography (CUSE): a novel method for two-dimensional shear elasticity imaging of soft tissues. IEEE Trans Med Imaging. 2012 Sep; 31(9):1821–32. [PubMed: 22736690]

8. Muthupillai R, Lomas D, Rossman P, Greenleaf J, Manduca A, Ehman R. Magnetic resonance elastography by direct visualization of propagating acoustic strain waves. Science (80-.). 1995 Sep; 269(5232):1854–1857.

9. Rump J, Klatt D, Braun J, Warmuth C, Sack I. Fractional encoding of harmonic motions in MR elastography. Magn Reson Med. 2007 Feb; 57(2):388–95. [PubMed: 17260354]

10. Glaser KJ, Manduca A, Ehman RL. Review of MR elastography applications and recent developments. J Magn Reson Imaging. 2012 Oct; 36(4):757–74. [PubMed: 22987755]

11. Hsu SJ, Bouchard RR, Dumont DM, Wolf PD, Trahey GE. In vivo assessment of myocardial stiffness with acoustic radiation force impulse imaging. Ultrasound Med Biol. 2007 Nov; 33(11): 1706–19. [PubMed: 17698282]

12. Pislaru C, Urban MW, Nenadic I, Greenleaf JF. Shearwave dispersion ultrasound vibrometry applied to in vivo myocardium. Conf Proc IEEE Eng Med Biol Soc. 2009 Jan.2009:2891–4. [PubMed: 19964051]

13. Pernot M, Couade M, Mateo P, Crozatier B, Fischmeister R, Tanter M. Real-time assessment of myocardial contractility using shear wave imaging. J Am Coll Cardiol. 2011 Jun; 58(1):65–72. [PubMed: 21700091]

14. Kolipaka A, McGee KP, Araoz PA, Glaser KJ, Manduca A, Romano AJ, Ehman RL. MR elastography as a method for the assessment of myocardial stiffness: comparison with an established pressure-volume model in a left ventricular model of the heart. Magn Reson Med. 2009 Jul; 62(1):135–40. [PubMed: 19353657]

15. Sack I, Rump J, Elgeti T, Samani A, Braun J. MR elastography of the human heart: noninvasive assessment of myocardial elasticity changes by shear wave amplitude variations. Magn Reson Med. 2009 Mar; 61(3):668–77. [PubMed: 19097236]

16. Robert B, Sinkus R, Gennisson J-L, Fink M. Application of DENSE-MR-elastography to the human heart. Magn Reson Med. 2009 Nov; 62(5):1155–63. [PubMed: 19780150]

17. Bouchard RR, Hsu SJ, Palmeri ML, Rouze NC, Nightingale KR, Trahey GE. Acoustic radiation force-driven assessment of myocardial elasticity using the displacement ratio rate (DRR) method. Ultrasound Med Biol. 2011 Jul; 37(7):1087–100. [PubMed: 21645966]

18. Couade M, Pernot M, Messas E, Bel A, Ba M, Hagege A, Fink M, Tanter M. In vivo quantitative mapping of myocardial stiffening and transmural anisotropy during the cardiac cycle. IEEE Trans Med Imaging. 2011 Feb; 30(2):295–305. [PubMed: 20851788]

19. Pislaru C, Urban MW, Pislaru SV, Kinnick RR, Greenleaf JF. Viscoelastic properties of normal and infarcted myocardium measured by a multifrequency shear wave method: comparison with pressure-segment length method. Ultrasound Med Biol. 2014 Aug; 40(8):1785–95. [PubMed: 24814645]

20. Pernot M, Fujikura K, Fung-Kee-Fung SD, Konofagou EE. ECG-gated, mechanical and electromechanical wave imaging of cardiovascular tissues in vivo. Ultrasound Med Biol. 2007 Jul; 33(7):1075–85. [PubMed: 17507146]

21. Provost J, Lee W-N, Fujikura K, Konofagou EE. Electromechanical wave imaging of normal and ischemic hearts in vivo. IEEE Trans Med Imaging. 2010 Mar; 29(3):625–35. [PubMed: 19709966]

22. Lu J-Y, Greenleaf JF. Pulse-echo imaging using a nondiffracting beam transducer. Ultrasound Med Biol. 1991 Jan; 17(3):265–281. [PubMed: 1887512]

23. Sandrin L, Catheline S, Tanter M, Hennequin X, Fink M. Time-Resolved Pulsed Elastography with Ultrafast Ultrasonic Imaging. Ultrason Imaging. 1999 Oct; 21(4):259–272. [PubMed: 10801211]

24. Tong L, Gao H, Choi HF, D'hooge J. Comparison of conventional parallel beamforming with plane wave and diverging wave imaging for cardiac applications: a simulation study. IEEE Trans Ultrason Ferroelectr Freq Control. 2012 Aug; 59(8):1654–63. [PubMed: 22899113]

25. Ekroll IK, Swillens A, Segers P, Dahl T, Torp H, Lovstakken L. Simultaneous quantification of flow and tissue velocities based on multi-angle plane wave imaging. IEEE Trans Ultrason Ferroelectr Freq Control. 2013 Apr; 60(4):727–38. [PubMed: 23549533]

26. Couade, M.; Pernot, M.; Tanter, M.; Messas, E.; Bel, A.; Ba, M.; Hagege, A-A.; Fink, M. Ultrafast imaging of the heart using circular wave synthetic imaging with phased arrays. 2009 IEEE International Ultrasonics Symposium; 2009. p. 515-518.

27. Song P, Zhao H, Urban M, Manduca A, Pislaru S, Kinnick R, Pislaru C, Greenleaf J, Chen S. Improved Shear Wave Motion Detection Using Pulse-Inversion Harmonic Imaging with a Phased Array Transducer. IEEE Trans Med Imaging. 2013 Sep. no. c.

28. Papadacci C, Pernot M, Couade M, Fink M, Tanter M. High-contrast ultrafast imaging of the heart. IEEE Trans Ultrason Ferroelectr Freq Control. 2014 Feb; 61(2):288–301. [PubMed: 24474135]

29. Whittingham, Ta. Tissue harmonic imaging. Eur Radiol. 1999 Jan; 9(Suppl 3):S323–6. [PubMed: 10602920]

30. Tranquart F, Grenier N, Eder V, Pourcelot L. Clinical Use of Ultrasound Tissue Harmonic Imaging. Ultrasound Med Biol. 1999; 25(6):889–894. [PubMed: 10461715]

31. Christopher T. Finite Amplitude Distortion-Based Pulse Echo Ultrasonic Imaging. IEEE Trans Ultrason Ferroelectr Freq Control. 1997; 44(1):125–139. [PubMed: 18244110]

32. Ma Q, Ma Y, Gong X, Zhang D. Improvement of tissue harmonic imaging using the pulse-inversion technique. Ultrasound Med Biol. 2005 Jul; 31(7):889–94. [PubMed: 15972194]

33. Doherty JR, Dahl JJ, Trahey GE. Harmonic tracking of acoustic radiation force-induced displacements. IEEE Trans Ultrason Ferroelectr Freq Control. 2013 Nov; 60(11):2347–58. [PubMed: 24158290]

34. Jensen JA, Nikolov SI, Gammelmark KL, Pedersen MH. Synthetic aperture ultrasound imaging. Ultrasonics. 2006 Dec; 44(Suppl 1):e5–15. [PubMed: 16959281]

35. Montaldo G, Tanter M, Bercoff J, Benech N, Fink M. Coherent plane-wave compounding for very high frame rate ultrasonography and transient elastography. IEEE Trans Ultrason Ferroelectr Freq Control. 2009 Mar; 56(3):489–506. [PubMed: 19411209]

36. Nikolov, SI.; Kortbek, J.; Jensen, JA. Practical applications of synthetic aperture imaging. 2010 IEEE International Ultrasonics Symposium; 2010. p. 350-358.

37. Luo J, Konofagou E. A fast normalized cross-correlation calculation method for motion estimation. IEEE Trans Ultrason Ferroelectr Freq Control. 2010 Jun; 57(6):1347–57. [PubMed: 20529710]

38. Provost J, Gambhir A, Vest J, Garan H, Konofagou EE. A clinical feasibility study of atrial and ventricular electromechanical wave imaging. Heart Rhythm. 2013 Jun; 10(6):856–62. [PubMed: 23454060]

39. McLaughlin J, Renzi D. Using level set based inversion of arrival times to recover shear wave speed in transient elastography and supersonic imaging. Inverse Probl. 2006; 22(2):707–725.

40. Deffieux T, Gennisson J-L, Larrat B, Fink M, Tanter M. The variance of quantitative estimates in shear wave imaging: Theory and experiments. IEEE Trans Ultrason Ferroelectr Freq Control. 2012; 59(11):2390–410. [PubMed: 23192803]

41. Konofagou EE, Provost J. Electromechanical wave imaging for noninvasive mapping of the 3D electrical activation sequence in canines and humans in vivo. J Biomech. 2012 Mar; 45(5):856–64. [PubMed: 22284425]

42. Kanai H. Propagation of spontaneously actuated pulsive vibration in human heart wall and in vivo viscoelasticity estimation. IEEE Trans Ultrason Ferroelectr Freq Control. 2005 Nov; 52(11):1931–1942. [PubMed: 16422405]

43. Papadacci C, Pernot M, Couade M, Fink M, Tanter M. Shear Wave Imaging of the heart using a cardiac phased array with coherent spatial compound. 2012 IEEE Int Ultrason Symp. 2012 Oct.: 2023–2026. no. c.

44. Denarie B, Tangen TA, Ekroll IK, Rolim N, Torp H, Bjåstad T. Coherent Plane Wave Compounding for Very High Frame Rate Ultrasonography of Rapidly Moving Targets. IEE Trans Med Imaging. 2013; 32(7):1265–1276.
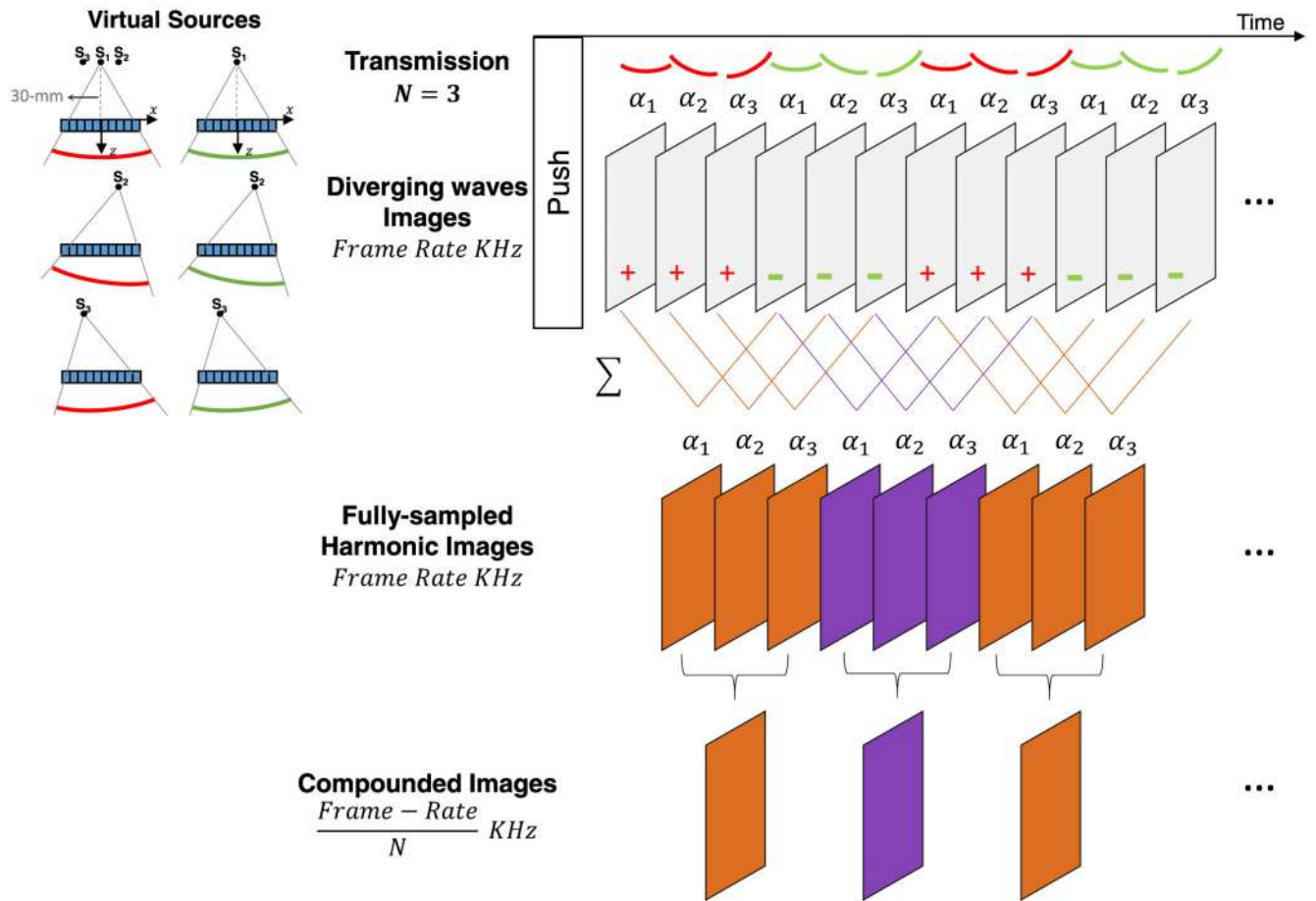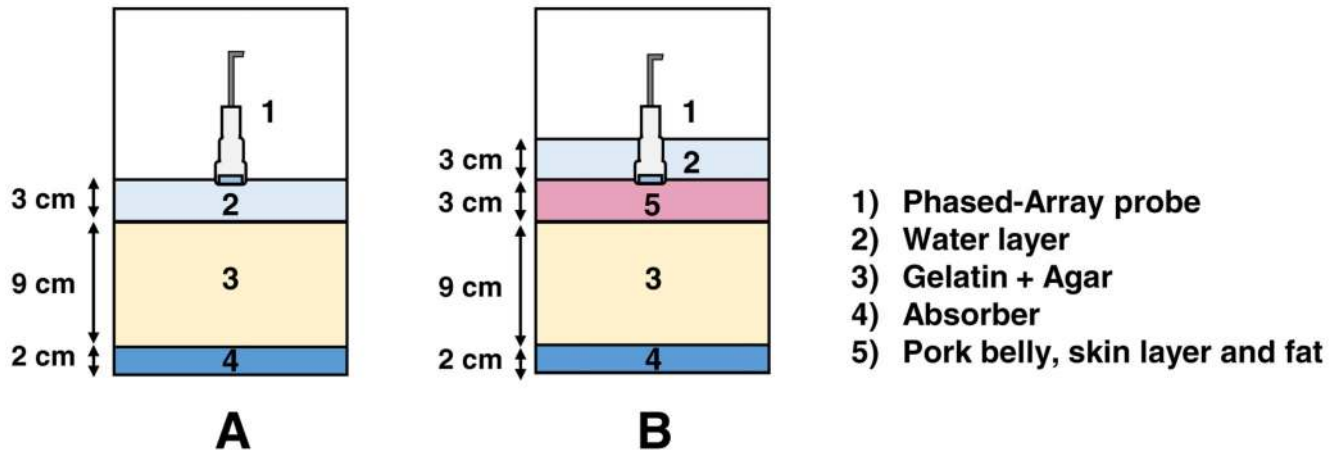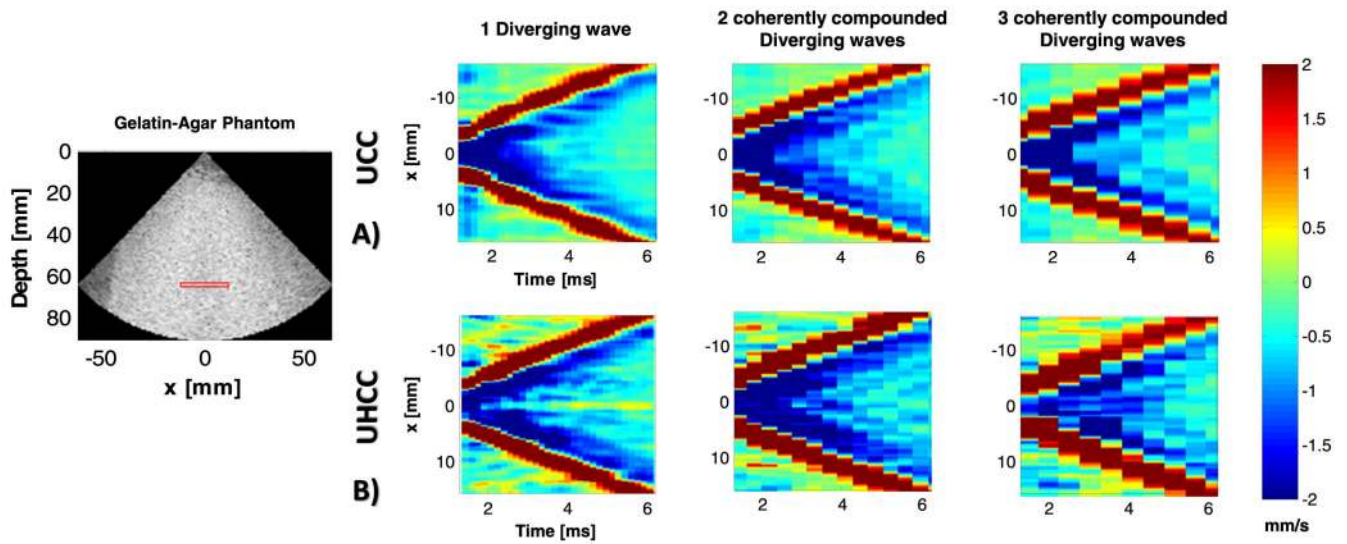
Figure 1.
UHCC Shear Wave Elastography sequence definition. Example of implementation of a sliding-window pulse-inversion harmonic technique and 3 coherently compounded diverging-waves.
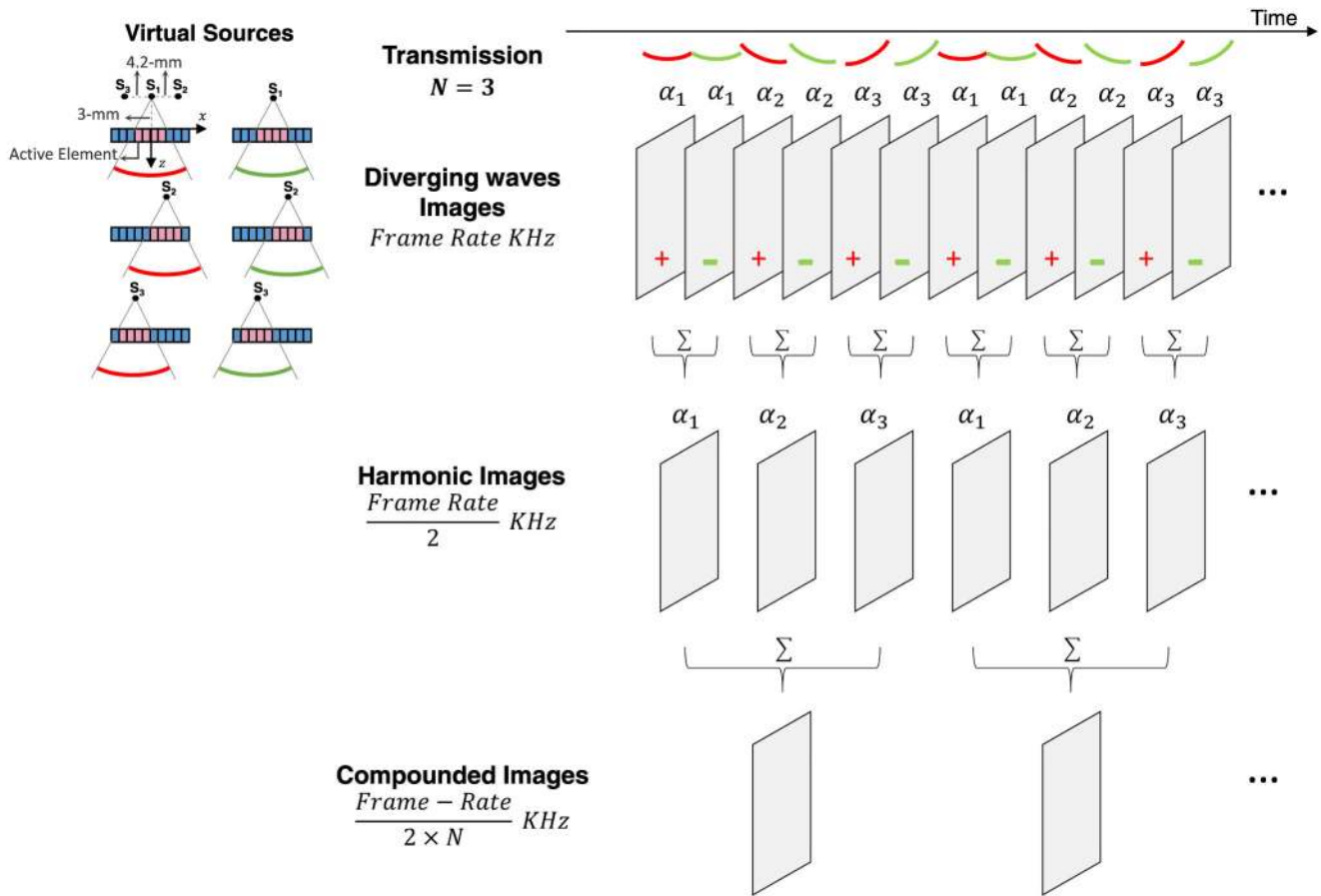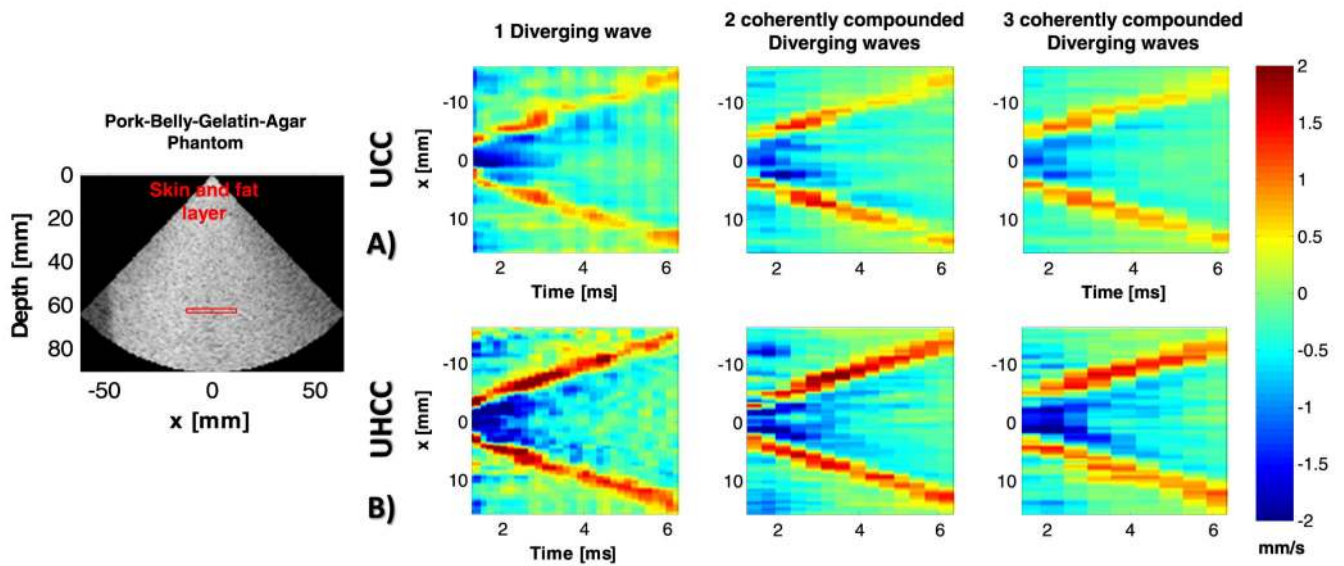
Figure 2.
UHCC B-mode sequence principle. Example with implementation of conventional pulse-inversion harmonic technique with 3 coherently compounded diverging-waves.
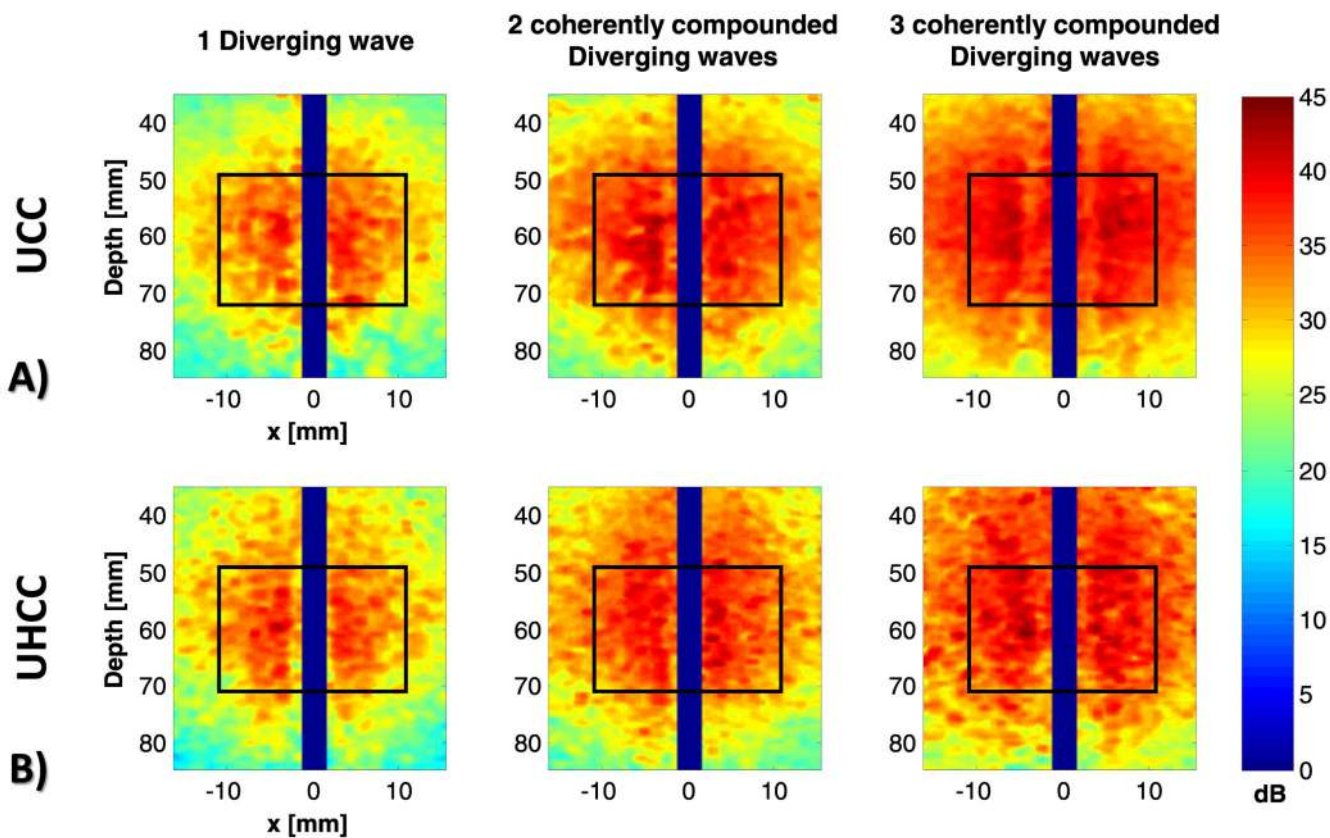
Figure 3.
In-vitro experimental apparatus. A) Gelatin-Agar phantom configuration; B) Pork-belly-gelation phantom configuration

Figure 4.
Gelatin-agar phantom configuration results. A UHCC B-mode image using 10 diverging-waves and B spatiotemporal tissue velocity images of the shear wave propagation (push-depth equal to 65 mm) for UHCC (B) and UCC (A) SWE using 1, 2, and 3 coherently compounded diverging waves. Tissue velocities were averaged axially within a 3-mm region.
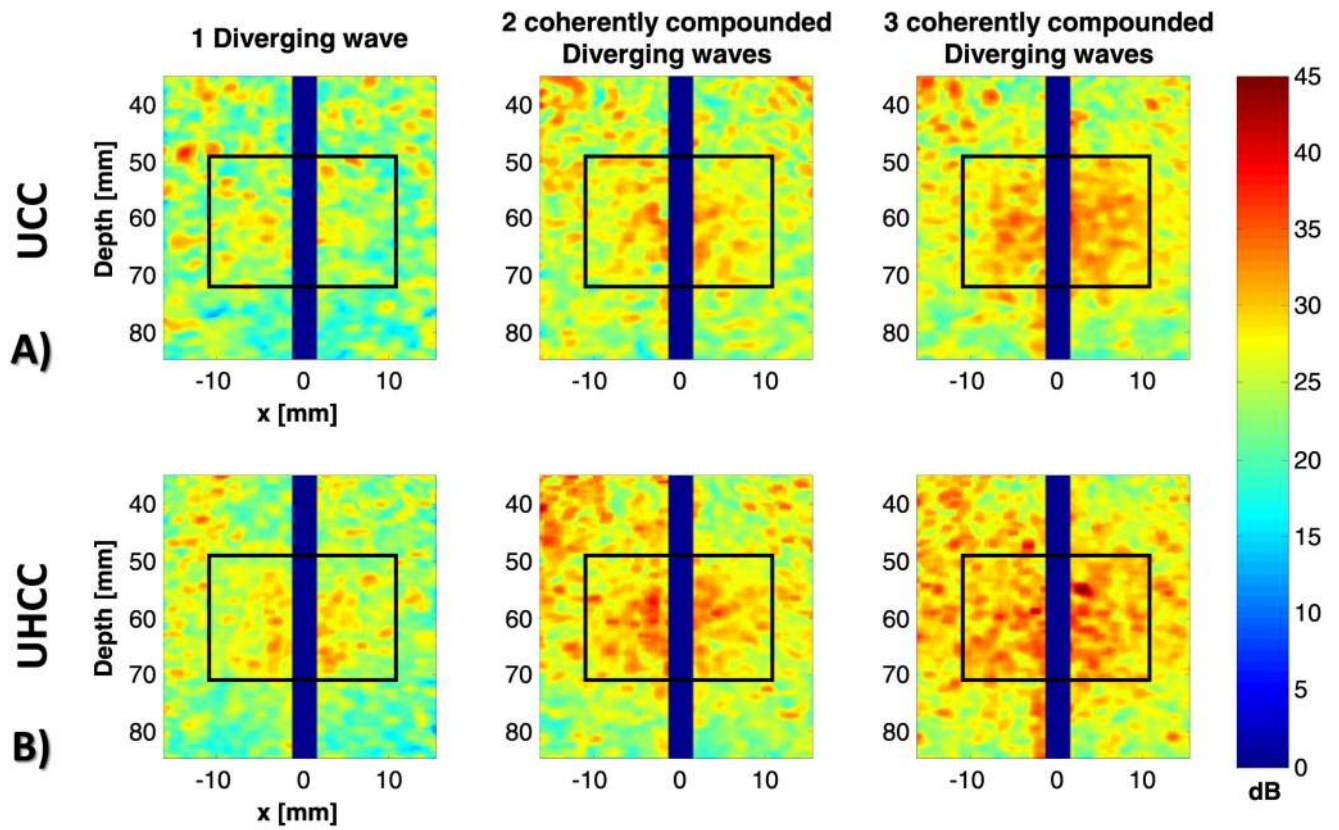
Figure 5.
Pork-belly-gelatin-agar phantom configuration results. A B-mode ultrafast harmonic using 10 diverging-waves and spatiotemporal tissue velocity images of the shear wave propagation (push-depth 65-mm) for UCC (A) and UHCC (B). SWE using 1, 2, and 3 coherently compounded diverging waves. Tissue velocities were averaged axially within a 3-mm region.

Figure 6.
SNR maps of gelatin-agar phantom configuration for UCC (A) and UHCC (B) imaging. The blue boxes represent the push region and the black rectangles represent the SNR regions-of-interest.
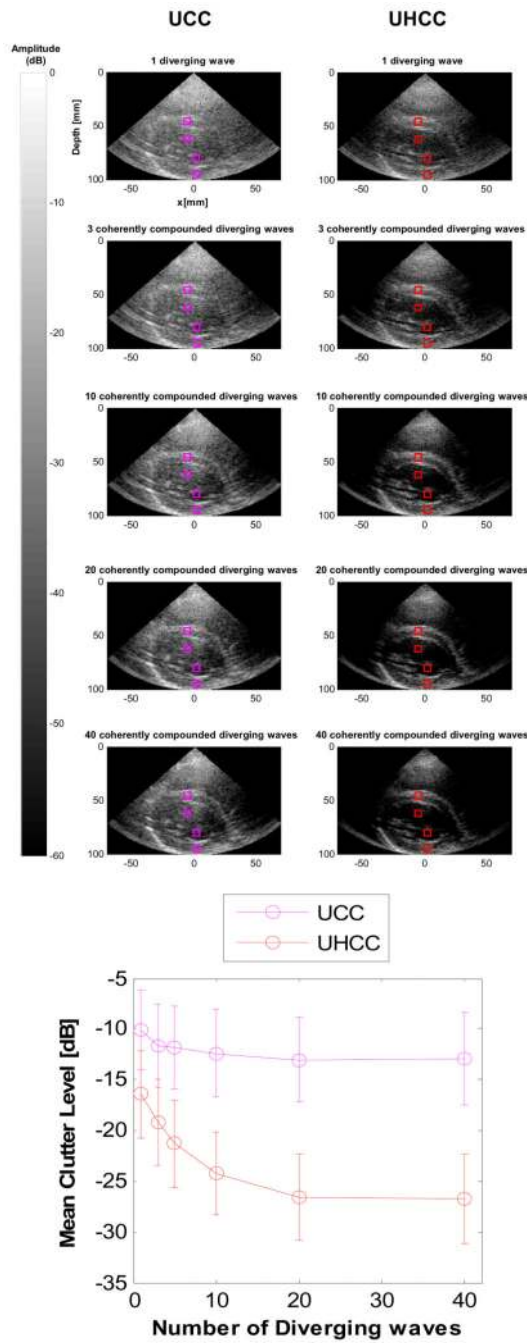
Figure 7.
SNR maps of Pork-belly-gelatin-agar phantom configuration for UCC (A) and UHCC (B) imaging. The blue boxes represent the push region and the black rectangles represent the SNR regions-of-interest.
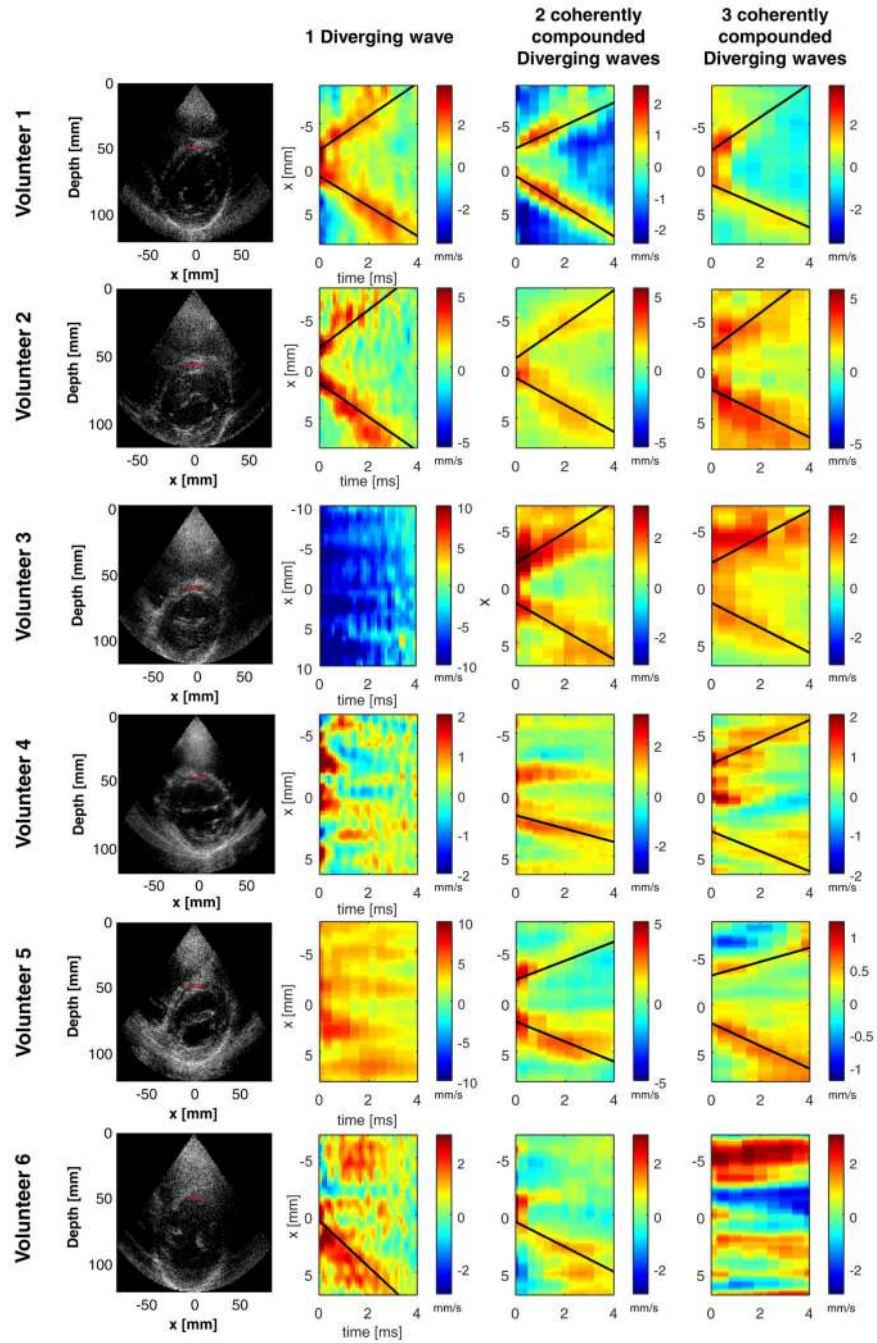
Figure 8.
In-vivo transthoracic UHCC SWE in the human heart of 6 volunteers at end-diastole. Left column: UHCC B-mode images acquired 5 ms before the SWE acquisition. Right columns: spatiotemporal tissue velocity maps of the shear wave propagation and averaged within 3-mm depth at the center of the myocardial wall for one (i.e. no coherent compound applied), two and three diverging-waves. The black lines represent the tracked shear wave propagation path. Its slope corresponds to the shear wave speed.

Figure 9.
UCC and UHCC B-mode images. Comparison using different number of diverging-waves. The average clutter signal level was evaluated in the anterior and posterior myocardium wall and left ventricle cavity (represented by the magenta and red boxes, for UCC and UHCC respectively).

Table 1

Parameters for in-vitro UCC and UHCC Imaging

Imaging Sequences Parameters	UCC SWE Imaging				UHCC SWE Imaging			
	Push	**UCC**			**Push**	**UHCC**		
Center frequency	2.75 – MHz	2.75 – MHz			2.75 – MHz	1.9 – MHz		
Number of Pushes	N = 1	---			N = 1	---		
Number of diverging-waves transmitted (N)	---	1 to 3			---	2 to 6		
Virtual sources axial position	---	30-mm			---	30-mm		
Subapertures length	19.2-mm	19.2-mm			19.2-mm	19.2-mm		
Pulse-repetition-frequency (PRF)	---	5924-Hz			---	5924-Hz		
Frame Rate (FR)	---	N = 1 5924-Hz	N = 2 2962-Hz	N = 3 1975-Hz	---	N = 2 5924-Hz	N = 4 2962-Hz	N = 6 1975-Hz
Acquisition duration	300-μs	20-ms max			300-μs	20-ms max		

Table 2

Parameters for in-vivo UHCC SWEI and UCC/UHCC B-mode Imaging

Imaging Sequences Parameters	SWE Imaging		B-mode Imaging	
	Push	**UHCC**	**UCC**	**UHCC**
Center frequency	2.75 – MHz	1.9 – MHz	2.75 – MHz	1.9 – MHz
Number of Pushes	N = 1	---	---	---
Number of diverging-waves transmitted (N)	---	2 to 6	1 to 40	2 to 80
Axial position of virtual sources	---	30-mm	3-mm	3-mm
Subapertures length	19.2-mm	19.2-mm	4.2-mm	4.2-mm
Pulse-repetition-frequency (PRF)	---	6849-Hz	5319-Hz	5319-Hz
Frame Rate (FR)	---	N = 2 6849-Hz / N = 4 3425-Hz / N = 6 1975-Hz	N = 1 5319-Hz / --- / N = 40 133-Hz	N = 2 260-Hz / --- / N = 80 67-Hz
Acquisition duration	300-µs	20-ms max	15-µs	15-ms max

Table 3

mean SNR of UHCC and UCC and SNR-percentage above 25 dB in the regions-of-interest for different number of Diverging-waves in the two phantom configurations

		1 Diverging-wave		2 Diverging-waves		3 Diverging-waves	
		SNR [dB]	Area % >= 25 dB	SNR [dB]	Area % >= 25 dB	SNR [dB]	Area % >= 25 dB
Gelatin-agar phantom	Fundamental	33.7	100.0	37.2	100.0	38.7	100.0
	Harmonic	33.7	95.6	36.5	100.0	38.0	100.0
Pork-belly-gelatin-agar phantom	Fundamental	25.7	47.1	28.4	88.4	30.2	95.9
	Harmonic	27.1	69.2	30.0	96.3	32.0	99.9

Table 4

Shear wave speed estimation for the six volunteers

Shear wave speed ± std* [m/s]	1 Diverging-wave				2 Diverging-waves				3 Diverging-waves			
	-x direction	$\bar{R}^2$	+x direction	$\bar{R}^2$	-x direction	$\bar{R}^2$	+x direction	$\bar{R}^2$	-x direction	$\bar{R}^2$	+x direction	$\bar{R}^2$
Volunteer 1	1.65 ± 0.42	0.83	1.11 ± 0.36	0.85	1.71 ± 0.22	0.91	1.15 ± 0.26	0.89	1.92 ± 0.13	0.95	1.13 ± 0.24	0.90
Volunteer 2	1.70 ± 0.37	0.85	1.26 ± 0.51	0.80	1.75 ± 0.17	0.93	1.17 ± 0.35	0.86	1.95 ± 0.14	0.95	1.11 ± 0.39	0.84
Volunteer 3	---	---	---	---	1.34 ± 0.33	0.86	1.23 ± 0.19	0.89	1.15 ± 0.32	0.86	1.09 ± 0.16	0.93
Volunteer 4	---	---	---	---	---	--	0.54 ± 0.19	0.92	0.81 ± 0.24	0.90	0.89 ± 0.27	0.89
Volunteer 5	---	---	---	---	0.95 ± 0.13	0.94	1.39 ± 0.48	0.80	0.72 ± 0.30	0.87	1.18 ± 0.23	0.91
Volunteer 6	---	---	1.86 ± 0.38	0.84	---	---	1.09 ± 0.38	0.84	---	---	---	---

*
std denotes for standard-deviation of the least-squares fit. Values with an adjusted R^2 inferior to 0.80 were excluded.

Table 5

Repeatability test of Shear Wave Velocity measurements on one Volunteer

Shear wave speed mean ± std[*] [m/s]	1 Diverging-wave		2 Diverging-waves		3 Diverging-waves	
	+x direction	-x direction	+x direction	-x direction	+x direction	-x direction
	1.88 ± 0.51	1.64 ± 0.30	1.44 ± 0.17	1.16 + 0.20	1.59 ± 0.44	1.31 ± 0.22

[*] std denotes for standard-deviation of the arithmetic mean.